CrystEngComm

ROYAL SOCIETY OF CHEMISTRY

PAPER

View Article Online
View Journal | View Issue

Cite this: *CrystEngComm*, 2024, **26**, 4812

Growth of GSAG:Ce scintillation crystals by the Bridgman method: influence of Ce concentration and codoping

K. L. Hovhannesyan,[a] M. V. Derdzyan,[a] G. Badalyan,[a] G. Kharatyan,[a] J. Pejchal,[b] M. Nikl,*[b] C. Dujardin*[cd] and A. G. Petrosyan*[a]

Received 15th June 2024,
Accepted 30th July 2024

DOI: 10.1039/d4ce00599f

rsc.li/crystengcomm

Single crystals of Ce-doped gadolinium scandium aluminum garnet ($Gd_3Sc_2Al_3O_{12}$; GSAG) with Ca^{2+}, Mg^{2+} and Li^+ co-dopants were grown by the Bridgman method. Regardless of melt composition, crystals tend to grow close to the congruent composition. Introduction of Ca^{2+} or Mg^{2+}, as in other Ce-doped garnets, leads to an increase of absorption below 350 nm, which may indicate formation of Ce^{4+} states, while no effect is seen with Li^+ co-doping. High Ce concentration and co-doping accelerate the scintillation rise and decay times; the codopants strongly significantly reduce the afterglow.

1. Introduction

The first paper on the Ce-doped gadolinium scandium aluminum garnet ($Gd_3Sc_2Al_3O_{12}$; GSAG) scintillator published in 1994 (ref. 1) reported an energy resolution of 12.5% at 662 keV, a scintillation decay time of 120 ns, a rise time of 60 ns and a light output of 30% relative to NaI(Tl); the single crystals were grown by the Czochralski method from melts with $Gd_{2.97}Ce_{0.03}Sc_2Al_3O_{12}$ composition. Substitution of scandium into the octahedral site of aluminum and gallium garnets was realized earlier in 1973 in order to achieve lattice parameters lying in the range suitable for their use as substrates for deposition of thin magnetic garnet layers.[2] Smaller lattice parameters of $Re_3Sc_2Al_3O_{12}$ (Re═Y, Sm–Yb) single crystals grown by the Czochralski method, as compared to lattice parameters of ceramic samples, indicated scandium substitution for the rare-earths and the true formula $\{Re_{3-x}Sc_x\}Sc_2Al_3O_{12}$. In electron paramagnetic studies of Mo^{3+} ions in $Y_3[Al_{2-x}Sc_x]Al_3O_{12}$ ($0 \leq x \leq 2$) crystals grown by the Bridgman method, an asymmetric signal shape was observed at $x = 2$, instead of a symmetric one, which should appear if all the eight Al^{3+} ions in the third coordination sphere of octahedral Mo^{3+} ions are replaced by Sc^{3+} ions. It was assumed that at large x, the ordered substitution of octahedral sites by Sc^{3+} is violated due to the location of some of the Sc^{3+} ions in dodecahedral sites. The measured lattice constant of $Y_3Sc_2Al_3O_{12}$ was noticeably smaller than the calculated value in the case of complete substitution of Al^{3+} ions by Sc^{3+} ions.[3]

On account of observed non-stoichiometry, melt composition $Gd_{2.9}Sc_{2.1}Al_3O_{12}$ was proposed and used in preparation of crystals by the Czochralski method.[2] A detailed study in later years[4] established that the congruent melt composition of GSAG corresponds to $Gd_{2.88}Sc_{1.89}Al_{3.23}O_{12}$. The homogeneity range of GSAG was also determined giving the permissible limits of redistribution of elements: Sc^{3+} ions may occupy all of the octahedral sites and Al^{3+} ions may occupy up to 20% of the sites, while the homogeneity range of Gd^{3+} is much narrower and is confined to within 2.85 to 2.93 formula units.[4] Thus, two of the three lattice sites in this garnet host are occupied jointly by two different cations.

In a recent paper,[5] single-phase transparent GSAG:Ce, GSAG:Ce,Mg and GSAG:Pr crystals were grown by a micro-pulling method using Ir and Mo crucibles and melts of congruent composition. The reported photoluminescence decay constant in GSAG:Ce (0.1 at%) is 41 ns but the scintillation decay under Cs-137 excitation is much slower (70–239 ns, depending on the composition and growth technology). The highest light yield value of 10 160 ph MeV^{-1} was achieved in GSAG:Ce (0.3%) grown in Mo crucibles in a reducing atmosphere and annealed in air to remove oxygen vacancies and related complex defects. EPMA analysis finally did not confirm a detectable Mo content. Single crystals of GSAG:Ce were also grown by the crucible-free floating zone method under a pure oxygen atmosphere which led to stabilization of Ce^{4+} states; but in terms of the light yield, the samples were inferior to those grown by the micro-pulling method.[6] The radiation tolerance of GSAG:Ce crystals with

[a] *Institute for Physical Research, National Academy of Sciences of RA, Ashtarak 0203, Armenia. E-mail: ashot.petrosyan783@gmail.com*
[b] *Institute of Physics of the Czech Academy of Sciences, 16200 Prague, Czech Republic. E-mail: nikl@fzu.cz*
[c] *Institut Lumière Matière UMR 5306 CNRS, Universite Claude Bernard Lyon 1, F-69622, Villeurbanne, France. E-mail: christophe.dujardin@univ-lyon1.fr*
[d] *Institut Universitaire de France (IUF), France*

co-dopants grown by the Bridgman method using Mo containers was reported in ref. 7. Under gamma-ray irradiation, compositions with the Li^+ co-dopant demonstrated induced absorption coefficient values (0.9 and 3.6 m^{-1} after 10 and 50 kGy doses, respectively) comparable to the values reported in other Ce-doped garnet scintillators (YAG:Ce, LuAG:Ce,[8] and GGAG:Ce).[9] Research on GSAG:Ce-related energy transfer between Gd^{3+} and Ce^{3+},[10] preparation of highly doped layers with high brightness for lighting applications[11] and transparent ceramic for high-power light emitting diodes was published as well.[12]

Despite the fact that the light yield of GSAG:Ce is inferior to those of other Ce-doped garnets (YAG:Ce, LuAG:Ce, and especially GGAG:Ce),[13] it nevertheless has some attractive qualities. Unlike gallium multicomponent garnets, it can be grown using Mo crucibles, instead of highly expensive Ir crucibles, and contains no volatile components and, consequently, no evaporation compensation in starting charge is needed. Another advantage of GSAG from the point of view of crystal growth is that the metal site is less compressed than that in LuAG or YAG[11] providing easier incorporation and higher solubility of Ce^{3+} and other rare-earths in this host. We also note that the low density and low effective atomic number of YAG restrict its application in high energy physics, while the dense LuAG contains a radioactive isotope ^{176}Lu (2.5% natural abundance). GSAG is a stable compound with a density of 5.82 g cm^{-3}, a hardness of 7.5 (Mohs value), a melting point of 1837 °C and a unit cell parameter of 12.395 Å.

The topic of co-dopants in Ce-doped oxide scintillators became very active after the first reports on their positive function in LSO:Ce,Ca(Mg)[14] and LuAG:Ce,Mg,[15] which stabilize the formation of Ce^{4+} providing faster scintillation response. After that, a large number of research was carried out on divalent (Ca^{2+}, Mg^{2+}) co-doping of several garnets (YAG:Ce,[16–21] LuAG:Ce,[18,22] GGAG:Ce (ref. 23–28)) to identify factors affecting the efficiency of $Ce^{3+} \rightarrow Ce^{4+}$ conversion and the defect structure. $Ce^{3+} \rightarrow Ce^{4+}$ conversion was also found in GAGG:Ce,Li (1 at%) grown by the Czochralski method with the compensation of the Li^+ excess negative charge attributed to both $Ce^{3+} \rightarrow Ce^{4+}$ conversion and effective formation of intrinsic lattice defects.[28] In YAG:Ce,Li (0.1–1 at%) grown by a micro-pulling method, it was found that (1) the Ce^{3+} content does not depend visibly on the Li concentration, (2) isolated O^- centers and O^- centers stabilized by neighbouring Li^+ are formed, as well as the concentration of oxygen vacancies is strongly increased, and (3) at low (0.1 at%) concentration, Li^+ ions substitute mainly for Y^{3+} ions, while at high (1 at%) concentration they substitute for Al^{3+} ions as well.[21] In YAG:Ce,Li grown by the Bridgman method, no site substitution by Li^+ was found at low (25–40 ppm) concentrations of Li^+, while at higher concentrations, Li^+ is forced into lattice sites.[18,20] In contrast to this, site substitution by Li^+ was found in LuAG:Ce,Li having a smaller unit cell volume and less size mismatch between involved cations.[18] The published experimental results on Li^+ codoping show that the incorporation and charge compensation mechanisms may differ depending on the concentration of Li^+, size misfit between Li^+ and host cations, the host unit cell volume, as well as the growth method. Studies of GSAG:Ce with co-dopants may contribute to the understanding of related mechanisms in other garnet hosts, as functions of listed factors.

In the present work, the growth of single crystals of the GSAG:Ce garnet with divalent and monovalent co-dopants by the Bridgman method is reported. Their optical absorption, radioluminescence, scintillation decay times and light yield were measured to characterize the grown materials. The incorporation behaviour and the functional role of Li^+, Ca^{2+} and Mg^{2+} co-dopant ions were discussed and compared to those in other Ce-doped garnets. The major crystal parameters affecting the light yield, scintillation decays and afterglow were identified.

2. Experimental section

2.1. Crystal growth

Single crystals were grown by the vertical Bridgman method. A modification of the method for the purpose of growing refractory oxides developed by Kh. S. Bagdasarov involves the use of thermal units made of Mo and W, cylindrical containers made of high-purity Mo and a reducing atmosphere.[29–31] The interaction with the crucible metal is limited to the dissolution of some amounts of Mo in the melts, some of which is absorbed by the crystal. According to measurements by electron paramagnetic resonance, the concentration of Mo^{3+} ions, which are localized exclusively at octahedral lattice sites, is 8.10^{-3} at% (measured in YAG[32]). Gd_2O_3 and CeO_2 of 99.99% purity, crystalline white sapphire (SPOLCHEMIE), and Sc_2O_3, MgO, $CaCO_3$, and Li_2CO_3 of 99.95% purity were used as starting components. Residual impurities of Si (50 ppm), Mn (6 ppm), and Fe (6 ppm) are mentioned in the quality certificate of Sc_2O_3. The rare-earth and transition metal residual amounts in Gd_2O3 and white sapphire are ≤1 ppm.

Single crystals doped with Ce, Ce:Li, Ce:Ca, Ce:Ca:Li, Ce:Mg, and Ce:Mg:Li with nominal concentrations of dopants of 0.5–1.0 at% (Ce), 50 ppm (Ca), 200 ppm (Mg), and 35–200 ppm (Li) were grown in an enclosed Ar/H_2 (10%) atmosphere at rates ≤ 2 mm h^{-1}. Seeds oriented along the ⟨100⟩ axis with typical dimensions of 1 mm in diameter and 35–40 mm long were used, which were cut from an undoped GSAG grown on a ⟨100⟩ oriented YAG seed. The obtained ~70 mm long and 13 mm in diameter crystals are bright yellow color turning to yellow-brown at increased Ce content (the undoped crystal is colorless). For the congruent melt composition, the crystals are single-phase, transparent and scatter-free along the full length. The end parts of the crystals grown from stoichiometric and $Gd_{2.9}Sc_{2.1}Al_3O_{12}$ melts at $g > 0.9$ contain 1 : 1 and 2 : 1 phases besides the garnet phase, while the main body is single-phase, transparent and scatter-free and, according to X-ray diffraction analysis, belongs to the cubic

garnet structure. Polished plates with dimensions of 0.2–2 × 8 × 8 mm^3 were prepared from the boules for further characterization. Fig. 1 shows some examples of grown crystals and cut plates.

2.2. Characterization methods

The crystal composition is measured on undoped samples by energy dispersive X-ray microanalysis (EDX) using an INCA Energy 300 instrument. The polished surfaces of the plates (d = 2 mm) were covered with carbon by thermal vacuum spraying. The absolute statistical errors in weight percent are: Gd (±0.35), Sc (± 0.16), and Al (±0.17). Absorption spectra were measured using a Specord200+ spectrophotometer in the range of 200–800 nm. Radioluminescence (RL) spectra and afterglow were measured using a custom-made spectrofluorometer 5000 M (Horiba Jobin Yvon) using a W X-ray tube (40 kV, 15 mA, Seifert) as an excitation source. The detection part of the setup involved a single-grating monochromator and a photon-counting detector TBX-04 (IBH Scotland). Measured RL spectra were corrected for the spectral dependence of detection sensitivity. A standard BGO scintillator sample plate of the same dimensions was used for the absolute intensity comparison. Scintillation light yield (LY) was determined by pulse height spectroscopy of scintillation response, using an HPMT (hybrid photomultiplier) model DEP PPO 475C, spectroscopy amplifier ORTEC model 672 (shaping time t = 1 μs) and multichannel buffer ORTEC 927TM. The sample was optically coupled to the HPMT using silicon grease; several layers of Teflon tape were placed over the sample as a reflector. Photoelectron yield (PhY) was obtained from the Gaussian fit of the photopeak in the pulse-height spectra. Quantum efficiency (QE) for each sample was calculated using RL spectra. Finally, light yield was calculated as LY = PhY/QE.

Decay time measurement under X-ray excitation was conducted using a time-correlated single photon counting system consisting of a fast photomultiplier tube (PMA-C-165) and PicoHarp 300 electronics operated at 128 ps per bin (Picoquant, Germany). The excitation source was an N5084 light-excited X-ray tube (Hamamatsu, Japan) operating at 30 kV. Optical excitation of the tube was achieved using a 500 kHz Horiba-Delta diode that emits light at 405 nm (DD-405-L). Instrumental response to the X-ray excitation pulse was about 100 ps. To select the desired emission wavelengths, we employed a Thorlabs FEL450 long-pass interference filter with a cut-off wavelength greater than 450 nm. The fitting function (the sum of three exponential terms) includes two decay components and one rising one (negative pre-exponential factor).

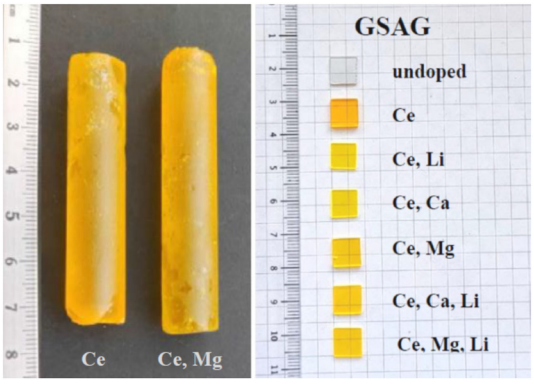

Fig. 1 Photographs of selected GSAG crystals and cut plates with different doping compositions.

3. Results and discussion

3.1. Crystal composition and dopant embedding

Composition in terms of formula units in the first and end portions of undoped crystals grown from melts of different compositions (stoichiometric, $Gd_{2.9}Sc_{2.1}Al_3O_{12}$, congruent) measured by EDX can be observed in Table 1.

As expected, the distribution of elements in the case of the congruent melt composition is uniform (Table 1: c), in agreement with ref. 4. For two other cases (Table 1: a and b), an increase in the Sc/Al ratio towards the crystal end is observed, which is smaller in the case of the stoichiometric melt. The tendency of increasing the Sc/Al ratio towards the end was observed in the GSAG:Cr laser crystal grown from the stoichiometric melt,[33] and in undoped GSAG grown from the $Gd_{2.9}Sc_{2.1}A1_3O_{12}$ melt,[4] both using the Czochralski method. The concentration of Gd in the case of the stoichiometric melt does not change and coincides with the concentration of the congruent melt.

In contrast to the micro-pulling growth method, for which the congruent melt composition was found to be the only acceptable one for the preparation of single-phase transparent materials,[5] the Bridgman and Czochralski methods are tolerant to some deviations from the congruent melt composition due to the large melt volume, increased contact between the crystal and the melt, efficient mixing and lower growth rates keeping the system much closer to the equilibrium. These factors ensure production of quality materials in a major part of the boules. Two further factors should be taken into account and additionally clarified when selecting the melt composition for the growth of doped crystals. The surface of heavily doped crystals grown by the Bridgman method from congruent melts becomes matte or rough, with small amounts of second phases in the very end portions. Quality degradation was mentioned in crystals grown by the Czochralski method from congruent melts with even low concentrations of rare-earth or Cr^{3+} ions requiring a specific correction of the melt composition.[4] Secondly, a higher tendency for cracking has been observed in crystals grown from congruent melts by the Bridgman method, which appears as longitudinal fissures or clefts on the {100} or {110} planes, similar to those observed in some cases in other garnets grown along the ⟨100⟩ axis.[34] We note that no differences were seen in the optical spectra and radiation tolerance between crystals grown from the three melt

Table 1 Composition of undoped GSAG crystals grown by the Bridgman method

	Melt composition								
	$Gd_3Sc_2Al_3O_{12}$ (a)			$Gd_{2.9}Sc_{2.1}Al_3O_{12}$ (b)			$Gd_{2.88}Sc_{1.89}Al_{3.23}O_{12}$ (c)		
	Crystal composition								
g	Gd	Sc	Al	Gd	Sc	Al	Gd	Sc	Al
0.1	2.91	2.08	3.01	2.89	1.95	3.16	2.91	1.88	3.21
0.9	2.91	2.14	2.95	2.93	2.09	2.98	2.91	1.89	3.20

g – a portion of the crystallized melt.

compositions. Measurements presented in the following sections were performed on samples cut out from crystals grown from stoichiometric melts. The nominal compositions for Ce-doped and multi-doped crystals can be specified as follows: (a) $Gd_{3(1-x)}$ $Ce_{3x}Sc_2Al_3O_{12}$, where x corresponds to the atomic fraction of Ce as follows: x = 0.005; 0.01, (b) $Gd_{3(1-x-y)}Ce_{3x}Ca_{3y}Sc_2Al_3O_{12}$, where x and y correspond to the atomic fractions of Ce and Ca, respectively: x = 0.005; 0.01 and y = 0.00035, (c) $Gd_{3(1-x)}Sc_{2(1-y)}Al_3O_{12}$, where x and y correspond to the atomic fractions of Ce and Mg, respectively: x = 0.005; 0.01 and y = 0.0035. Other compositions are calculated in the same way, and assuming that lithium goes into the octahedral sites.

3.2. Absorption spectra

Absorption spectra of undoped and Ce-doped GSAG with concentrations of Ce^{3+} in the range of 0.4–0.94 at% can be observed in Fig. 2a. The onset of the host band edge is at around 220 nm.

Absorption lines corresponding to 4f–4f transitions of Gd^{3+} ions at ~250 nm, ~275 nm and ~310 nm, related to $^8S_{7/2} \rightarrow {}^6D_j$, $^8S_{7/2} \rightarrow {}^6I_j$ and $^8S_{7/2} \rightarrow {}^6P_j$ transitions, respectively, are present in the spectra. The peaks at 449 nm and 341 nm and the broad shoulder at 235 nm belong to 4f–$5d_1$, 4f–$5d_2$ and 4f–$5d_{3,4,5}$ transitions of Ce^{3+}, respectively. The absorption spectra are identical to those measured in crystals grown by the micro-pulling method.[5]

Absorption spectra of GSAG:Ce with Li^+, Ca^{2+}, Mg^{2+} and Ca^{2+}:Li^+ codopants and close Ce^{3+} concentrations can be observed in Fig. 2b. The Ca^{2+} and Mg^{2+} co-dopants induce the stabilization of the Ce^{4+} center, evidenced in the increase of absorption below 330 nm related to the charge transfer absorption of Ce^{4+}, indicating site occupation by Ca^{2+} and Mg^{2+} ions, as observed in other garnets.[15,18,23] The spectra of GSAG:Ce and GSAG:Ce,Li coincide, indicating a weak or no interaction between Li^+ and Ce^{3+}.

The change in the concentration of Li^+ in the range of 35–200 ppm barely influences the spectrum shape (Fig. 2c), suggesting the preferential location of Li^+ ions at an interstitial position with no interaction with Ce^{3+}.

Substitution by Li^+ for Sc^{3+} could be expected, since the ionic radii of Li^+ and Sc^{3+} ions are very close ($r_{Sc^{VI}}$ = 0.745 Å; $r_{Li^{VI}}$ = 0.76 Å). Considering the sizes in the tetrahedral coordination ($r_{Li^{IV}}$ = 0.59 Å; $r_{Al^{IV}}$ = 0.39 Å), the concentration of Li^+ in these sites is expected to be low. The unit cell volume of GSAG is larger than that of both GAGG and YAG. No indication of the substitution of Li^+ at octahedral sites suggests that the size fit is a less important factor for the substitution of one ion by another, when the charge misfit is −2, and the unit cell volume becomes a determining parameter for either site occupation or interstitial location of Li^+, as assumed in the works on GGAG:Ce,Li, *e.g.* in ref. 26. It

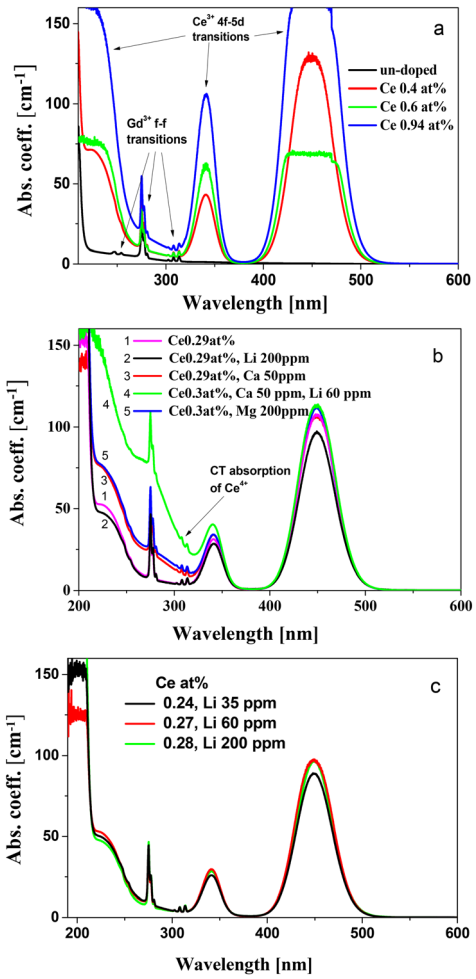

Fig. 2 Absorption spectra of (a) undoped GSAG and GSAG:Ce, (b) GSAG:Ce with similar measured Ce^{3+} concentrations and containing co-dopants, and (c) GSAG:Ce with different Li^+ contents. Flattening of the absorption peak around 450 nm in (a) is an experimental artifact due to sample luminescence.

can be expected that at low concentrations, the Li^+ co-dopant would be located preferentially in interstitial spaces in garnets with a unit cell volume equal or larger than that of YAG with charge compensation due to a decrease in the concentration of oxygen vacancies. Better radiation resistance of the Li^+ co-doped GSAG:Ce crystal indicated a reduction of defects.[7] Other factors should be considered, when finally stating the incorporation type of Li^+, such as preference of Li^+ for a particular coordination in compounds or the possibility of cluster (Ce^{4+}–Li^+) formation not resulting in enhancement of absorption below 350 nm.[28]

It can be observed in Fig. 2b that the joint introduction of Ca,Li into GSAG:Ce leads to a higher concentration of Ce^{4+}, as compared to that into Li-free GSAG:Ce,Ca. Such a synergistic effect for Ce valence conversion was earlier observed in YAG:Ce co-doped with both Ca^{2+} and Li^+ and supported by scintillation decay time measurements.[19] In this case, other possible ways of charge compensation (*e.g.* O^- center and oxygen vacancy formation) may be prevented.

3.3. Scintillation characteristics

In the radioluminescence spectra under CW X-ray excitation of the undoped crystal, the Gd^{3+} emission lines at 275 nm (from ^6I_x) and 311 nm (from ^6P_x) and several characteristic emissions of accidental impurities coming from raw materials are identified, namely those of Tb^{3+}, Ce^{3+}, Eu^{3+} and (possibly) Fe^{3+} (Fig. 3a).

In the Ce-doped samples, the RL spectra are dominated by the Ce^{3+} emission band ($5d_1$–4f transition) comparable with the amplitude of the BGO standard scintillator (Fig. 3b). The highest LY values are obtained for the uncodoped samples with a maximum of 10 240 ph MeV^{-1} (129% of BGO standard LY) for a Ce concentration of 0.6%. Li-codoping does not noticeably affect LY values, while codoping with divalent ions (Ca,Mg) results in somewhat decreased LY values, as shown in Table 2.

The afterglow characteristics are shown for the selected samples in Fig. 4 and the values (10 ms after X-ray cut-off) are in Table 2.

In the case of afterglow, the worst performance is shown by the Ce-doped samples, codoping by Li improves/decreases the afterglow by at least one order of magnitude, and further decreased (about 2×) values are achieved for the Ca codopant. The double (Ca,Li) or (Mg,Li) codoped samples perform a little worse (about 2×) compared to the Li codopant itself, see Table 2. In general, an afterglow lower than 0.1% is considered to be very low and satisfactory for most of applications where afterglow is an important parameter.

Scintillation decay analysis required the fitting function in the form of the sum of three exponential terms providing one rise time (negative pre-exponential factor) and two decay times which are reported in Table 2. The time at 1/*e* of the decay amplitude is also reported since it combines the effect of all time constants and exponential term amplitudes. Three

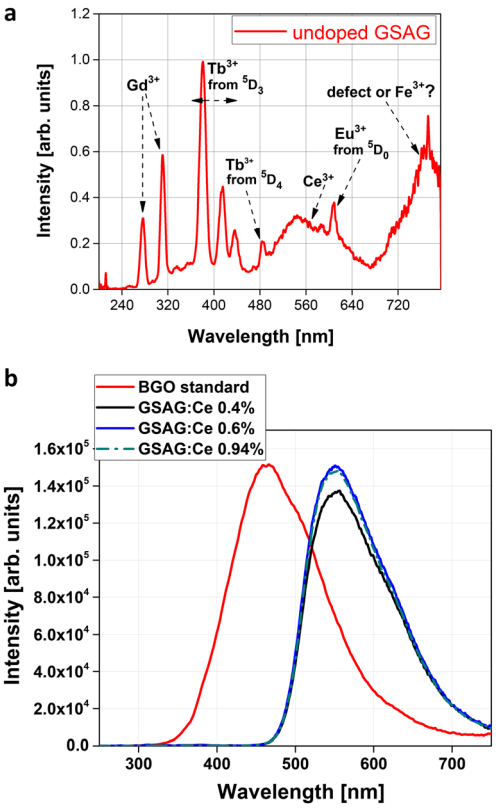

Fig. 3 (a) Radioluminescence spectra of the undoped GSAG sample. (b) RL spectra of the Ce-doped GSAG samples in absolute comparison with a BGO standard scintillator.

illustrative decays are presented in Fig. 5. They are representing low and high Ce concentrated samples. This highlights the wide range of rise and decay times that have been observed, from 15 to 45 ns for the rise and from 27 to 76 ns for the first decay component.

To visualize the trends, the calculated scintillating parameters have been plotted only as a function of the Ce content, and various codoping combinations are represented by different colors in Fig. 6.

Fig. 6a–d clearly demonstrate that in the landscape of combination of tested codoping, only the cerium concentration show a major effect on the time constant. Increasing the Ce concentration is accelerating noticeably the scintillation response both in the rising and falling parts (a factor of 3 is observed from the lowest to the highest concentration in time@1/*e*). Fig. 6e demonstrates that the cerium concentration does not affect the scintillation yield. We can conclude that the acceleration of rise and decay times is not related to quenching but rather to more effective energy transfer from the host and the change of branching ratios between the components. Fig. 6f shows that codoping of any kind improves afterglow. To summarize the ensemble of parameters, the best figure of merit (speed of response, scintillation yield and afterglow) appears for highest Ce concentration with Mg^{2+} codoping with a light yield of 9320 photons per MeV and a 1/*e* decay time of 41.2 ns.

Table 2 Light yield values, decay times τ_1–τ_2 (ns) and rise times τ_r (ns), time@1/*e* and afterglow levels at 10 ms after X-ray cut-off are summarized. The light yield value of a BGO standard is measured as 7930 ph MeV^{-1}

Sample	L.Y (ph MeV^{-1})	τ_1–τ_2 (ns)	Rise time τ_r (ns)	Time@1/*e* (ns)	Afterglow (%)
GSAG:Ce					
GdScAG–Ce 0.4%	**8550**				
GSAG–Ce0.4%	**8550**	58–281	45	299.2	0.5
GSAG–Ce0.6%	**10 240**	46–184	27	232.5	2.0
GSAG-Ce0.94%	**9280**	32–121	18	175.8	4.8
GSAG:Ce + Li					
GSAG Ce0.23%, Li 60 ppm	**9530**	113–438	43	332.8	0.06
GSAG Ce0.27%, Li 60 ppm	**9430**	88–353	43	282.1	0.03
GSAG Ce0.34%, Li 60 ppm	**9340**	68–298	41	250.9	0.03
GSAG Ce0.38%, Li 35 ppm	**8960**	66–277	38	234.4	0.04
GSAG Ce0.8%, Li 100 ppm	**6820**	32–137	27	188.6	0.18
GSAG:Ce + Ca					
GSAG Ce0.25%, Ca 50 ppm	**8620**	76–323	45	271.5	0.02
GSAG Ce0.29%, Ca 50 ppm	**9100**	61–281	43	243.1	0.03
GSAG Ce0.38%, Ca 50 ppm	**8770**	46–214	36	209.2	0.03
GSAG Ce0.45%, Ca 50 ppm	**8550**	41–183	32	179.5	0.05
GSAG:Ce + Ca + Li					
GSAG Ce0.24%, Ca 50 ppm, Li 60 ppm	**6420**	44–208	38	202.3	0.05
GdScAG Ce0.3%, Ca50 ppm, Li 60 ppm	**8550**	37–152	26	145.9	0.05
GSAG Ce0.36%, Ca50 ppm, Li 60 ppm	**6160**	33–148	29	151.3	0.1
GSAG:Ce + Mg					
GSAG Ce0.9%, Mg 200 ppm	**8430**	32–112	18	109.1	0.05
GSAG Ce1,3%, Mg 200 ppm	**9320**	27–92	16	91.4	0.05
GSAG:Ce + Mg + Li					
GSAG Ce1, 3%, Mg 200 ppm, Li 100 ppm	**8690**	27–91	15	92.7	0.05

4. Conclusions

Single crystals of various codoped $Gd_3Sc_2Al_3O_{12}$:Ce were grown by the Bridgman method and characterized, namely the undoped crystals, Ce-doped crystals, and co-doped crystals with Ca^{2+}, Mg^{2+}, Li^+, Mg^{2+}:Li^+ and Ca^{2+}:Li^+ . Owing to the configuration of the Bridgman method, high quality single crystals could be grown from melts slightly differing in composition from the congruent melt. We have observed that the Ca^{2+} and Mg^{2+} codopants induce the stabilization of the Ce^{4+} center, evidenced in the increase of absorption below 330 nm related to the charge transfer absorption of Ce^{4+}, indicating cation site occupation by Ca^{2+} and Mg^{2+}. It appears that the timing parameters measured under X-rays are mainly dependent on the cerium concentration, while the afterglow is improved by at least a factor of 20 by the

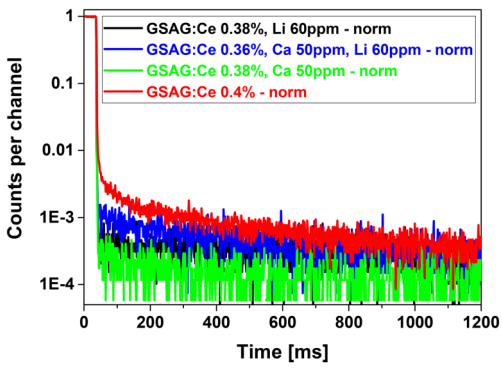

Fig. 4 Afterglow of selected samples (see legend). Excitation by X-ray (40 kV, 1 min).

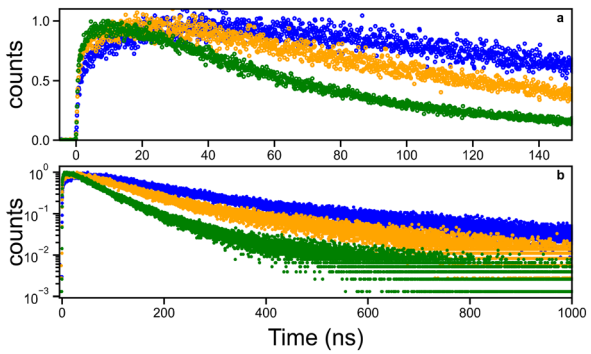

Fig. 5 X-ray excited decays measured for GSAG Ce0.25%, Ca 50 ppm (blue), GSAG Ce0.45%, Ca 50 ppm (orange) and GSAG Ce1,3%, Mg 200 ppm (green). Figure (a) corresponds to the first 150 ns to highlight the rise time and figure (b) corresponds to the first 1000 ns.

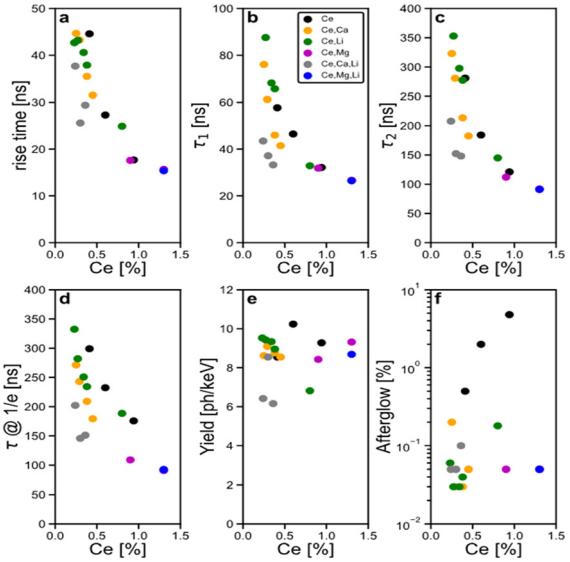

Fig. 6 Evolution of the scintillation parameters as a function of the Ce concentration: (a) rise time (ns), (b) τ_1 (ns), (c) τ_2 (ns), (d) τ @ 1/*e* (ns), (e) light yield (ph keV^{-1}), (f) afterglow (%). Black color points show the single Ce doping, orange ones the Ca^{2+} codoping, green ones the Li^{+} codoping, purple ones the Mg^{2+} codoping, grey ones the double Ca^{2+} + Li^{+} codoping and blue ones the double Mg^{2+} + Li^{+} codoping.

codopants (in the best samples, the afterglow is 0.03%). The absorption spectra of GSAG:Ce and GSAG:Ce,Li (with the Li+ concentration taken in a wide (35–200 ppm) range) coincide, indicating a weak or no interaction between Li^{+} and Ce^{3+} and suggesting the preferential location of Li^{+} at an interstitial position. This is the case despite the very small size misfit between Li^{+} and Sc^{3+} ions in the six-fold coordination, and it is assumed that the large unit cell volume of GSAG is the most critical in the incorporation mechanism of Li^{+} ions. Li-codoping does not noticeably affect LY, while codoping with divalent ions (Ca,Mg) results in the decrease of the LY values, as previously observed in other Ce-doped garnet hosts. The highest LY values are obtained for uncodoped samples with a maximum of 10 240 ph MeV^{-1} (129% of BGO LY) in GSAG:Ce (0.6 at%). Nevertheless, the combination of all scintillating parameters allows us to conclude that the best performing composition is the Mg^{2+} codoped sample with the highest Ce concentration of 1.3%.

Data availability

One figure is photos of crystals, and 3 figures are in "Origin" format with all related data available.

Conflicts of interest

There are no conflicts to declare.

Acknowledgements

This work was supported by the State Committee of Science of the Ministry of Education and Science of the Republic of Armenia grant no. 21AG-1C030. The authors acknowledge the CNRS for their financial support under the International Research Program (IPR) "Scintlab". Partial support from the Czech Science Foundation grant no. 21-17731S is acknowledged.

References

1 A. Kling, D. Kollewe and D. Mateika, *Nucl. Instrum. Methods Phys. Res., Sect. A*, 1994, **346**, 205.
2 C. Brandle and R. Barns, *J. Cryst. Growth*, 1973, **20**, 1.
3 G. Asatryan, A. Kuzanyan, A. Petrosyan, E. Sharoyan and G. Shirinyan, *Solid State Phys.*, 1987, **20**, 586.
4 G. Lutts, A. Denisov, E. Zharikov, A. Zagumennyi, S. Kozlikin, S. Lavrishchev and S. Samoylova, *Opt. Quantum Electron.*, 1990, **22**, S269.
5 O. Zapadlík, J. Pejchal, R. Kučerková, A. Beitlerová and M. Nikl, *Cryst. Growth Des.*, 2021, **21**, 7139.
6 F. Zajíc, J. Pospíšil, R. Kučerková, P. Boháček and M. Nikl, *CrystEngComm*, 2024, **627**, 127479.
7 K. L. Hovhannesyan, M. V. Derdzyan, I. A. Ghambaryan, T. I. Butaeva, C. Dujardin and A. G. Petrosyan, *Phys. Status Solidi A*, 2023, **220**, 2300386.
8 M. T. Lucchini, K. Pauwels, K. Blazek, S. Ochesanu and E. Auffray, *IEEE Trans. Nucl. Sci.*, 2016, **63**, 586.
9 M. T. Lucchini, V. Babin, P. Blazek, S. Gundacker, K. Kamada, M. Nikl, A. Petrosyan, A. Yoshikawa and E. Auffray, *Nucl. Instrum. Methods Phys. Res., Sect. A*, 2016, **816**, 176.
10 U. Happek, J. Choi and A. M. Srivastava, *J. Lumin.*, 2001, **94**, 7.
11 L. Devys, G. Dantelle, G. Laurita, E. Homeyer, I. Gautier-Luneau, C. Dujardin, R. Seshadri and T. Gacoin, *J. Lumin.*, 2017, **190**, 62.
12 Y. Ma, L. Zhang, J. Huang, R. Wang, T. Li, T. Zhou, Z. Shi, J. Li, Y. Li, G. Huang, Z. Wang, F. A. Selim, M. Li, Y. Wang and H. Chen, *Opt. Express*, 2021, **29**(6/15), 9474.
13 C. Dujardin, E. Auffray, E. Bourret, P. Dorenbos, P. Lecoq, M. Nikl, A. N. Vasil'ev, A. Yoshikawa and R. Zhu, *IEEE Trans. Nucl. Sci.*, 2018, **65**, 1977.
14 S. Blahuta, A. Bessiere, B. Viana, P. Dorenbos and V. Ouspenski, *IEEE Trans. Nucl. Sci.*, 2013, **60**, 3134.
15 M. Nikl, K. Kamada, V. Babin, J. Pejchal, K. Pilarova, E. Mihokova, A. Beitlerova, K. Bartosiewicz, S. Kurosawa and A. Yoshikawa, *Cryst. Growth Des.*, 2014, **14**, 4827.
16 A. Nagura, K. Kamada, M. Nikl, S. Kurosawa, J. Peichal, Y. Yokota, Y. Ohashi and A. Yoshikawa, *Jpn. J. Appl. Phys.*, 2015, **54**, 04DH17.
17 P. Dickens, D. T. Haven, S. Friedrich and K. G. Lynn, *J. Cryst. Growth*, 2019, **507**, 16.
18 M. V. Derdzyan, K. L. Hovhannesyan, A. V. Yeganyan, R. V. Sargsyan, A. Novikov, A. G. Petrosyan and C. Dujardin, *CrystEngComm*, 2018, **20**, 1520.
19 K. L. Hovhannesyan, M. V. Derdzyan, A. Novikov, A. G. Petrosyan and C. Dujardin, *Phys. Status Solidi B*, 2020, **257**, 2000243.
20 M. V. Derdzyan, K. L. Hovhannesyan, A. Novikov, E. Auffray, A. G. Petrosyan and C. Dujardin, *Phys. Status Solidi B*, 2019, **256**, 1800724.

21 V. V. Laguta, M. Buryi, V. Babin, P. Machek, S. Zazubovich, K. Bartosiewicz, S. Kurosawa, A. Yamaji, A. Yoshikawa, K. Ulicna, V. Chlan, H. Stepankova and M. Nikl, *J. Mater. Chem. C*, 2023, **11**, 1346.
22 K. Kamada, M. Nikl, S. Kurosawa, A. Beitlerova, A. Nagura, Y. Shoji, J. Pejchal, Y. Ohashi, Y. Yokota and A. Yoshikawa, *J. Cryst. Growth*, 2016, **452**, 85.
23 M. Lucchini, V. Babin, K. Blazek, S. Gundacker, K. Kamada, M. Nikl, A. Petrosyan, A. Yoshikawa and E. Auffray, *Nucl. Instrum. Methods Phys. Res., Sect. A*, 2016, **186**, 176.
24 G. Dantelle, G. Boulon, Y. Guyot, D. Testemale, M. Guzik, S. Kurosawa, K. Kamada and A. Yoshikawa, $Gd_3Al_2Ga_3O_{12}$ garnet crystals, *Phys. Status Solidi A*, 2020, **257**, 1900510.
25 K. Kamada, Y. Shoji, V. V. Kochurikhin, M. Yoshino, S. Okumara, S. Yamamoto, J. Yeom, S. Kurosawa, Y. Yokota, Y. Ohashi, M. Yoshino and A. Yokishawa, *Opt. Mater.*, 2017, **65**, 52.
26 W. Chewpraditkul, N. Pattanaboonmee, O. Sakthong, K. Wantong, W. Chewpradiktul, A. Yoshikawa, K. Kamada, S. Kurosawa, T. Szczesniak, M. Moszynski, V. Babin and M. Nikl, *Opt. Mater.*, 2019, **92**, 181.
27 M. Yoshino, K. Bartosiewicz, T. Horiai, K. Kamada, A. Yamaji, Y. Shoji, Y. Yokota, S. Kurosawa, Y. Ohashi, H. Sato, S. Toyoda, R. Kucerkova, V. Jary, M. Nikl and A. Yoshikawa, *Phys. Status Solidi B*, 2020, **257**, 1900504.
28 S. Zazubovich, V. V. Laguta, P. Machek, K. Kamada, A. Yoshikawa and M. Nikl, *Faguang Xuebao*, 2022, **242**, 118548.
29 Kh. S. Bagdasarov, *High-temperature crystallization from melt*, Yerevan, edit print 2003, p. 180 – ISBN 99941-36-16-x.
30 Kh. S. Bagdasarov, in *Modern Crystallography III, Section Crystal Growth*, Springer-Verlag, Berlin, Heidelberg, New York, Tokyo, 1984.
31 A. G. Petrosyan, *J. Cryst. Growth*, 1994, **139**, 372.
32 E. A. Markosyan, A. G. Petrosyan and E. G. Sharoyan, *Solid State Phys.*, 1973, **8**, 2504.
33 J. Drube, G. Huber and D. Mateika, in *Springer Series in Optical Sci.*, New York, 1980, vol. 52, p. 118.
34 A. G. Petrosyan, G. O. Shirinyan, K. L. Ovanesyan and A. S. Kuzanyan, *J. Cryst. Growth*, 1981, **52**, 556.